ADVANCED OPTICAL MATERIALS
www.advopticalmat.de

Ultra-Narrowband Metamaterial Absorbers for High Spectral Resolution Infrared Spectroscopy

*Sungho Kang, Zhenyun Qian, Vageeswar Rajaram, Sila Deniz Calisgan, Andrea Alù, and Matteo Rinaldi**

Metamaterial perfect absorbers (MPAs) are artificial materials composed of an array of subwavelength structures that manipulate electromagnetic waves to achieve extraordinary light absorption properties. Driven by the advent of the Internet of Things, MPAs are employed in microelectromechanical systems for the development of efficient and miniaturized IR detectors, imagers, and spectrometers, thanks to their lithographically tunable peak absorption, spectral selectivity, and ultrathin thickness. MPAs characterized by high absorptance in narrow spectral bands are particularly desirable for the implementation of high-resolution IR spectroscopic sensors. Yet, no accurate analytical model is currently available to guide the design of an MPA with ultra-narrow absorption bandwidth, while meeting all the stringent requirements for spectroscopic sensors. Here, a circuit model capable of accurately predicting spectral responses of metal–insulator–metal (MIM) IR absorbers is reported. The model is experimentally validated in the mid-wavelength IR spectral range and exploited for the first demonstration of an MIM IR absorber that exhibits performance approaching the predicted physical limits: full-width at half-maximum ≈3% and near-unity absorption ($\eta > 99.7\%$) at 5.83 μm wavelength, while independent of incident angle and polarization of the impinging IR radiation. These unprecedented absorption properties are key enablers for the development of miniaturized, low-cost, and high-resolution spectrometers.

IR absorption spectroscopy is a powerful technique to identify and study chemicals of various kinds in a nondisruptive way, and it is employed in multidisciplinary fields, such as medical, industrial, or military applications.[1] Specifically, in the mid- to long-wavelength IR regime, the fundamental rotational–vibrational modes of chemical compounds exhibit strong absorption or emission of electromagnetic energy in distinctively narrow spectral bands, which are commonly exploited for spectroscopic chemical fingerprinting.[2–4] In IR absorption spectroscopy systems, the characteristic IR responses of a sample are recorded by a detector, which typically relies on a highly IR-absorbing material. Spectrally selective IR absorbers, in particular, are key components for implementing compact IR spectroscopy systems, as they completely eliminate the need of additional narrowband filter elements to discriminate spectral regions of interest.[5–7] The achievement of high absorptance in a narrow spectral band is particularly important for IR spectroscopy, since multiple chemical species may exhibit strongly confined spectral emission/absorption bands closely located to each other (e.g., λ_0 = 4.25 and 4.5 μm for carbon dioxide and nitrous oxide, respectively). Moreover, both the acceptance angle and polarization sensitivity of the absorbers play a significant role in maximizing the total absorption, especially for noninvasive standoff chemical sensing applications, where the chemical compounds are inherently spread over a wide field of view with arbitrary orientations of molecular structures, resulting in random incident angles and polarizations.

Recently, due to the burgeoning development of miniaturized sensors with the advent of Internet of Things, the demand for compact IR sensor arrays capable of addressing multiple wavelengths in a small form factor has been steadily growing. The key challenge lies in realizing multispectral absorber arrays that are lithographically defined and monolithically integrated

S. Kang, Dr. Z. Qian, V. Rajaram, S. D. Calisgan, Prof. M. Rinaldi
Department of Electrical and Computer Engineering
Northeastern University
360 Huntington Avenue, Boston, MA 02115, USA
E-mail: rinaldi@ece.neu.edu
S. Kang, Dr. Z. Qian, V. Rajaram, S. D. Calisgan, Prof. M. Rinaldi
Northeastern SMART Center
409 Interdisciplinary Science and Engineering Complex
360 Huntington Avenue, Boston, MA 02115, USA
The ORCID identification number(s) for the author(s) of this article can be found under https://doi.org/10.1002/adom.201801236.

DOI: 10.1002/adom.201801236

Prof. A. Alù
Photonics Initiative
Advanced Science Research Center
City University of New York
85 St. Nicholas Terrace, New York, NY 10031, USA
Prof. A. Alù
Physics Program
The Graduate Center
City University of New York
365 Fifth Avenue, New York, NY 10016, USA
Prof. A. Alù
Department of Electrical Engineering
City College of City University of New York
New York, NY 10031, USA

on the same chip, with a minimized footprint. This challenge has been tackled in the field of plasmonics and metamaterials—a rapidly growing research field that has enabled the design of materials with optical properties not found in nature, which allows overcoming the diffraction limit and focus light in deeply subwavelength volumes. Plasmonic IR absorbers, in particular, leverage the strong light–matter interaction enabled by surface plasmons (SPs) at deeply subwavelength scales to achieve ideal absorber responses.[8,9] For instance, a number of recently proposed plasmonic IR absorbers exploit strong SP resonances at metal–dielectric interfaces to demonstrate distinctively narrow absorption bands suitable for high spectral resolution spectroscopic applications, while maintaining high absorptance and lithographically tunable spectral absorption bands in a subwavelength form factor.[10–14] Nevertheless, their fixed acceptance angle and dependence on polarization cause a significantly lower total absorption compared to the bulk material counterpart, making them unable to meet all the stringent requirements suitable for miniaturized spectroscopy systems.

Metal–insulator–metal (MIM) IR nanostructured absorbers, on the other hand, are characterized by lithographically controlled tunability of the absorption wavelength and near-unity absorption with little constraints on angle or polarization.[9,15–18] MIM absorbers confine localized SPs in a 2D mode within a subwavelength trilayer geometry consisting of an array of plasmonic nanostructures and a ground metal layer separated by a thin dielectric spacer.[19] The strong 2D plasmon excitation of fourfold symmetric nanostructures ensures a response with minimal constraints on the property of incident IR waves (i.e., angle and polarization), while maintaining spectrally selective near-unity absorption.[19,20] Surely enough, these characteristics have made these absorbers ideal candidates for a new class of plasmonically enhanced IR sensing microsystems, such as spectrally selective microbolometers, nano-/microelectromechanical system (N/MEMS) resonance IR sensors, and micromechanical photoswitches.[21–30] Nevertheless, there has been no experimental realization of ultra-narrowband MIM IR absorbers specifically tailored for IR spectroscopy. In fact, early reports have shown full-width at half-maximum (FWHM) only as narrow as ≈15% using MIM IR absorbers with suitably shaped nanostructures (e.g., square or circular patches, holes, or crosses), which fall short from the required spectral resolution for IR spectroscopy.[15,16,31] We attribute this limitation to the absence of analytical tools capturing the physics of the system with respect to the parameters defined by the constituent materials and geometry. It is worthwhile to mention that experimental demonstrations of MIM IR absorbers in more recent reports have highlighted narrower FWHM (<5%); yet such performance increase was not guided by a generalized analytical design method that directly relates absorption properties to the characteristic parameters (i.e., geometric dimensions and materials) of MIM IR absorbers, which is particularly important when designing an absorber with specific process constraints, such as lithography limits or material compatibility.[20,30] In fact, many analytical models reported to date fail to investigate absorption, spectral bandwidths, and resonant wavelengths of the MIM IR absorbers in a concise and accurate form.[15,17,32–36]

Here, we present the design and experimental verification of ultra-narrow bandwidth metamaterial absorbers that simultaneously meet all stringent constraints for IR spectroscopic applications: 1) full-width at half-maximum reaching its theoretical limit (FWHM ≈ 3%); 2) near-unity absorption ($\eta > 99.7\%$); 3) wide lithographic tunability ($\lambda_0 = 4$–7 µm); and 4) angle and polarization insensitivity. We propose an improved lumped equivalent circuit model based on work by Sakurai et al. to take the effect of electric dipole resonance between neighboring unit cells into consideration, which contributes to the off-resonance reactance.[33,34] The new circuit model provides an accurate description of the effective surface impedance, which we use in a transmission-line model to analytically derive accurate spectral response of the MIM IR absorbers. By analyzing the proposed circuit model, we find that optimization of the length-to-width ratio and periodicity of the cross-shaped nanostructures is crucial to realize high absorption with narrow spectral resolution. Our 12 sets of fabricated narrowband MIM IR absorbers demonstrate ultra-narrow absorption bandwidths, near-perfect absorption, and wide lithographical tunability, while maintaining angle and polarization insensitivity. Lastly, the potential impact of the proposed devices on mid-wavelength IR (MWIR) gas spectroscopy applications is presented by comparing the absorption spectra of the proposed devices with the emission spectra of four different trace-gas molecular species.

The proposed ultra-narrow bandwidth IR absorbers are composed of an array of gold (Au) nanostructures and a continuous ground layer separated by a subwavelength thickness

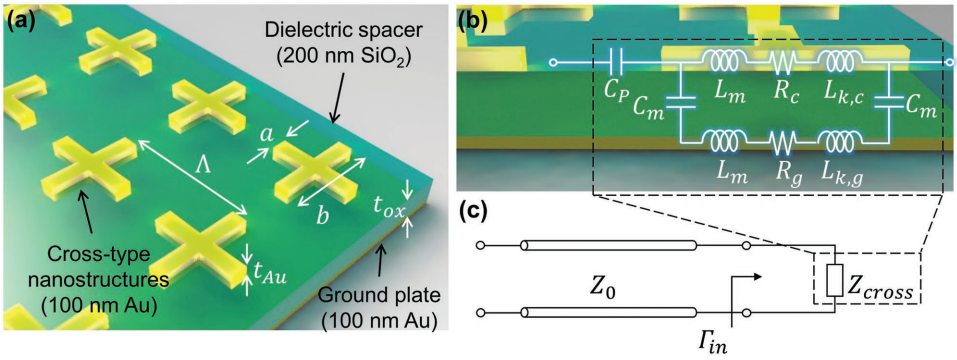

Figure 1. Ultra-narrow bandwidth MIM IR absorber and lumped equivalent circuit model. a) 3D schematic of the proposed MIM IR absorber. b) Cross-sectional view of the MIM IR absorber with lumped equivalent circuit model. c) Transmission-line model of the MIM IR absorber.

silicon dioxide (SiO_2) layer (**Figure 1**a). The top nanostructures are cross-shaped, with lateral dimensions denoted as a (width), b (length), and Λ (periodicity). The thickness of SiO_2 (t_{ox} = 200 nm) and Au (t_{Au} = 100 nm) was appropriately chosen for strong SP confinement and a wide lithographical tunability of the spectral absorption band in MWIR (λ_0 = 4–7 μm). It is worth noting that a different dielectric thickness is required for optimized performance beyond this spectral range. When the electromagnetic waves in a specific spectral band impinge on the absorber, the electric dipole resonance (Figure S1a, Supporting Information) is excited in the array of nanostructures, inducing antiparallel currents on the ground layer via plasmonic coupling in the subwavelength dielectric gap. As indicated by the magnetic field intensity ($|H|$), the current loop gives rise to a strong magnetic field confinement (Figure S1b, Supporting Information). With the right level of loss to support critical coupling and conjugate matching, near-unity absorption is achieved at the designed spectral band.

In order to achieve ultra-narrow spectral selectivity and near-unity absorption, we analyze the peak absorptance and FWHM of the fundamental resonance mode with respect to the geometric and material parameters. Our lumped equivalent circuit model (Figure 1b) serves as a powerful tool to analyze the spectral responses and to design MIM IR absorbers without the need of time-consuming numerical optimization. Sakurai et al. initially proposed an RLC equivalent circuit model to describe the magnetic response of the MIM IR absorbers.[33,34] As this model comprises the lumped circuit elements as functions of width, length, and dielectric spacing, it provides a helpful understanding of the magnetic resonance condition with respect to the physical parameters of the MIM IR absorber. Therefore, it can be used to predict the wavelength at which maximum absorption occurs. Nevertheless, the model lacks the capability to accurately predict the actual absorptance, bandwidth, and angular response of the MIM IR absorber. We attribute this shortcoming to the absence of the off-resonance reactance from the capacitive coupling between neighboring unit cells. The additional reactance is modeled as a capacitor in the modified circuit to provide an accurate description of the effective surface impedance (Z_{cross}) of the absorbers. The accurate circuit-based description of the MIM IR absorbers is utilized in a transmission-line model to predict the condition for critical coupling and conjugate impedance matching that leads to a strong absorption (Figure 1c). To validate the lumped equivalent circuit model and design optimization, the results are directly compared with experimental results.

The modified lumped equivalent circuit (Figure 1b) consists of a periodic coupling capacitance (C_P) in series with an additional RLC circuit branch, which models the magnetic dipole resonance. While C_P contributes to the electric dipole resonance and the out-of-resonance impedance level, the near-field coupling of localized plasmons and current loop are described in the magnetic dipole branch. C_P originates from the capacitive coupling between neighboring cross-shaped nanostructures, and it is approximated by the capacitance between two neighboring wires (Equation (1)).[37] The magnetic dipole branch consists of a pair of mutual and kinetic inductances (L_m and L_k) and gap capacitances (C_m) as well as the resistance of two gold layers (R). L_m and C_m take the forms of Equations (2) and (3), respectively, where ε_0 (≈8.854 × 10^{-12} F m^{-1}) and μ_0 (=4π × 10^{-7} H m^{-1}) are permittivity and permeability of free space, respectively, and ε_{ox} is the relative permittivity of silicon dioxide.[38] Note that c (=0.4–0.5) is a constant appropriately chosen to take the fringe effect of the capacitance and nonuniform electric field distribution into consideration (Figure S2, Supporting Information).[33,34] The values of the effective lumped elements, determined using quasi-static considerations, are[39–42]

$$C_P = \pi\varepsilon_0 \frac{a}{\ln\left(\frac{2(\Lambda-b)}{t_{Au}} + \sqrt{\left(\frac{2(\Lambda-b)}{t_{Au}}\right)^2 - 1}\right)} \quad (1)$$

$$L_m = \frac{1}{2}\mu_0 \frac{t_{ox} b}{a} \quad (2)$$

$$C_m = c\varepsilon_0\varepsilon_{ox} \frac{b}{2}\frac{a}{t_{ox}} \quad (3)$$

The above quasi-static expressions for the lumped elements assume waves impinging at normal incidence. Nevertheless, they can be expressed for an oblique incident angle by replacing the geometric dimensions ($\Lambda - b$ and t_{ox}) with effective parameters (Equations (S1)–(S3), Supporting Information). R and L_k in the magnetic dipole branch arise from the real and imaginary parts of impedance of the gold layers, respectively (Equations (S3)–(S8), Supporting Information). Since the current distributions in the gold layers are dependent upon geometrical parameters, we distinguish between the resistance (R_c) and kinetic inductance ($L_{k,c}$) of the cross-nanostructures from those of the continuous ground plane (R_g and $L_{k,g}$). Note that the effective length ($b' = c' \times b$) of the cross-nanostructures is smaller than the designed length (b) due to the uneven current distribution, and it needs to be corrected by a numerical factor ($c' = 1 - c \approx 0.6$) to accurately model R_c and $L_{k,c}$ in Equations (4) and (5) (Figure S2, Supporting Information).[33,34] On the other hand, the current distribution of the continuous ground plane is shown in Figure S2 in the Supporting Information and results in an effective width of 0.5b, given in Equations (6) and (7). The plasma frequency ($\omega_p \approx 2\pi \times 2.183 \times 10^{15}$ rad s^{-1}) and relaxation time ($\tau_{Au} \approx 12.4 \times 10^{-15}$ s) of gold are obtained from Rakić et al. and are used to calculate the penetration depth (δ_{Au}) and DC conductivity (σ_{Au}) as described in Equations (8) and (9), where λ and κ are the wavelength in free space and the extinction coefficient of gold, respectively[43–45]

$$L_{k,c} = \frac{c'b}{a\delta_{Au}}\frac{1}{\varepsilon_0\omega_p^2} \quad (4)$$

$$R_c = \frac{c'b}{a\delta_{Au}}\frac{1}{\sigma_{Au}} \quad (5)$$

$$L_{k,g} = \frac{b}{0.5b\delta_{Au}}\frac{1}{\varepsilon_0\omega_p^2} \quad (6)$$

$$R_g = \frac{b}{0.5b\delta_{Au}}\frac{1}{\sigma_{Au}} \quad (7)$$

$$\delta_{Au} = \frac{\lambda}{2\pi\kappa} \tag{8}$$

$$\sigma_{Au} = \varepsilon_0 \omega_p^2 \tau_{Au} \tag{9}$$

It is worth noting that all lumped circuit elements are expressed in terms of geometric variables (a, b, t_{Au}, and Λ) and material properties (ε_{ox}, ω_p, and τ_{Au}), which can guide the design and optimization of the absorbers. Finally, based on a conventional transmission-line model to describe the interaction with the impinging wave, we can calculate the absorptance (A) as $A = 1 - R_{in}$, where R_{in} ($=|\Gamma_{in}|^2 = |(Z_{cross} - Z_0)/(Z_{cross} + Z_0)|^2$) is the reflectance and Z_0 ($=\sqrt{(\mu_0/\varepsilon_0)} \approx 377\ \Omega$) is the impedance of free space. When the value of Z_{cross} is close to the free space impedance ($Z_{cross} \approx Z_0$), R_{in} approaches zero, leading to near-unity absorption. For oblique incidence, as the wave impedance is modified, the effective surface impedance also changes, yielding robust angular response, which is described in more detail in Section 2 of Supporting Information.

Due to the frequency-dependent lumped circuit elements and nonreal Z_{cross}, it is not feasible to obtain exact closed-form solutions in terms of circuit parameters for the FWHM and f_{peak} using transmission-line theory. However, one can estimate FWHM by evaluating the quality factor (Q) of the circuit ($Q \propto R_{eq}C_{eq}/L_{eq}$, where R_{eq}, C_{eq}, and L_{eq} are equivalent resistance, capacitance, and inductance of the circuit, respectively), and f_{peak} by equating the imaginary part of Z_{cross} to zero (Equations (S9)–(S12), Supporting Information). They can be further simplified and expressed in terms of geometric and material parameters of the cross-type absorbers (Equations (10) and (11))

$$\mathrm{FWHM} \propto R\frac{C_p}{L_m + L_k} \propto \frac{a}{\tau_{Au}\ln(\Lambda)} \tag{10}$$

$$f_{peak} \propto \sqrt{\frac{1}{C_m(L_m + L_k)}} \propto \frac{1}{b} \tag{11}$$

Equation (10) indicates that one can achieve narrow FWHM by maximizing Λ while reducing the width (a). However, the upper limit of Λ is set by the wavelength of operation (i.e., $\Lambda < \Lambda_{max} = \lambda_{peak}/(1 + \sin\theta)$, where $0 < \theta < 90°$ is the angle of incidence), for Λ exceeding the limit will result in diffraction and the lumped equivalent circuit model is no longer valid.[46–50] Note that this limit is more stringent (smaller Λ_{max}) at oblique incidence ($\theta > 0$), making the device more susceptible to diffraction. Therefore, to ensure strong absorption over a wide acceptance angle, we choose $\theta = 30°$ for the upper limit of Λ (e.g., $\Lambda_{max} \approx 4$ μm for $\lambda_{peak} = 6$ μm). **Figure 2**a shows that an absorber with a wider Λ reaching its limit of 4 μm results in a significant improvement

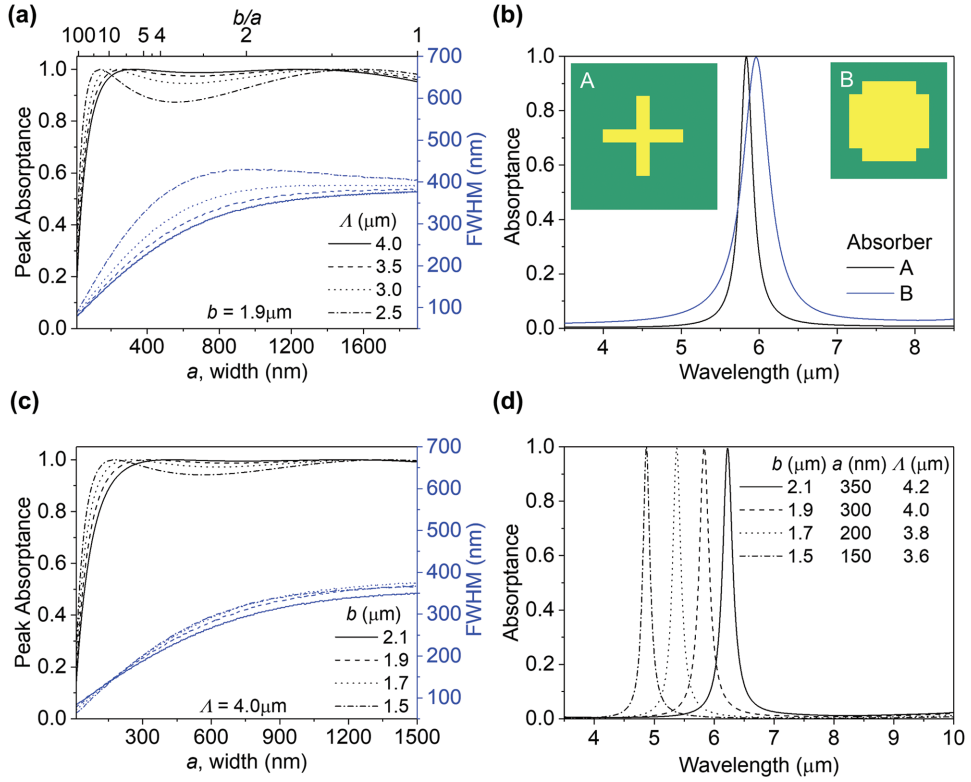

Figure 2. Optimization of MIM IR absorbers for high spectral resolution spectroscopy. a) Calculated peak absorptance and FWHM with respect to the width and periodicity. b) Comparison of the calculated absorption responses of the two MIM IR absorbers with different width and periodicity. The insets illustrate the geometric configurations of a unit cell for absorber A and absorber B. The lateral dimensions of absorber A (B) are as follows: b = 1900 nm (1900 nm), a = 300 nm (1700 nm), and Λ = 4.0 μm (2.5 μm). c) Calculated peak absorptance and FWHM with respect to the width and length. d) Calculated absorption responses of the lithographically tuned MIM IR absorbers with optimized geometric dimensions.

with up to 20% in spectral selectivity (∝1/FWHM). Furthermore, it implies that one can decrease FWHM by reducing a (i.e., larger b/a), up to the point when the absorption starts to decrease due to impedance mismatch ($Z_{cross} \gg Z_0$ with smaller a), which sets the limit of scaling for a. In other words, when designing an optimized MIM IR absorber with a high spectral selectivity, both FWHM and absorption must be considered simultaneously. Since f_{peak} can be independently tuned by b, there exists a set of Λ and a at a given f_{peak} that guarantees a narrow FWHM and a near-unity absorption. Indeed, the MIM IR absorber with a larger periodicity (Λ = 4.0 μm) and a narrower width (a = 200 nm) demonstrates a significantly better spectral selectivity than the one with a smaller periodicity (Λ = 2.5 μm) and a wider width (a = 1700 nm) (Figure 2b). We attribute this performance improvement based on geometric optimization to the minimization of cross-talk (due to the excessive capacitive coupling) between neighboring nanostructures (i.e., large Λ) and high length-to-width ratio (b/a) for strong plasmonic coupling and electromagnetic field confinement. In fact, wider absorption bandwidths (FWHM > 20%) have been commonly reported based on patch- or circular-type MIM IR absorbers, due to their relatively narrow Λ and b/a ratio.[15,27]

Twelve sets of MIM IR absorbers were fabricated and characterized on the same substrate, with lateral dimensions (a, b, and Λ) as the only variables (**Figure 3**a). The geometric parameters of each absorber are optimized to achieve high selectivity based on our model (Table S1, Supporting Information). Since the peak frequency is inversely proportional to the length (b) and almost independent of other dimensions (Equation (11)), the peak wavelength can be lithographically tuned by choosing an appropriate b while consistently maintaining a narrowband absorption. Note that all fabricated devices consistently demonstrate high absorptance (η > 90%) and narrow bandwidth (FWHM < 4%) over a wide spectral region (λ_0 = 4–7 μm) (Figure 3b). The top plasmonic nanostructures were patterned via lift-off resist (LOR)-assisted electron beam lithography, followed by evaporation of 10–100 nm Ti–Au. The LOR-assisted lithography step here is crucial to obtain the smooth edges without lift-off residues (Figure 3c), which are commonly seen in standard single-layer lift-off process. The details of the fabrication process, including cross-sectional schematics and characterization of LOR-assisted electron beam lithography, are described in Figure S4 of the Supporting Information. Figure 3d highlights that an absorption bandwidth of only 180 nm (FWHM = 3.1% at λ_0 = 5.83 μm), the narrowest reported to date, and near-perfect absorption (η > 99.7%) are simultaneously obtained, while strong reflectance ($\eta \approx$ 0%) is achieved in the out-of-band spectral region. It is also worth noting that the lumped equivalent circuit model and the transmission line theory accurately predict the spectral response of the absorber from which one can obtain the bandwidth, peak wavelength, and absorptance levels.

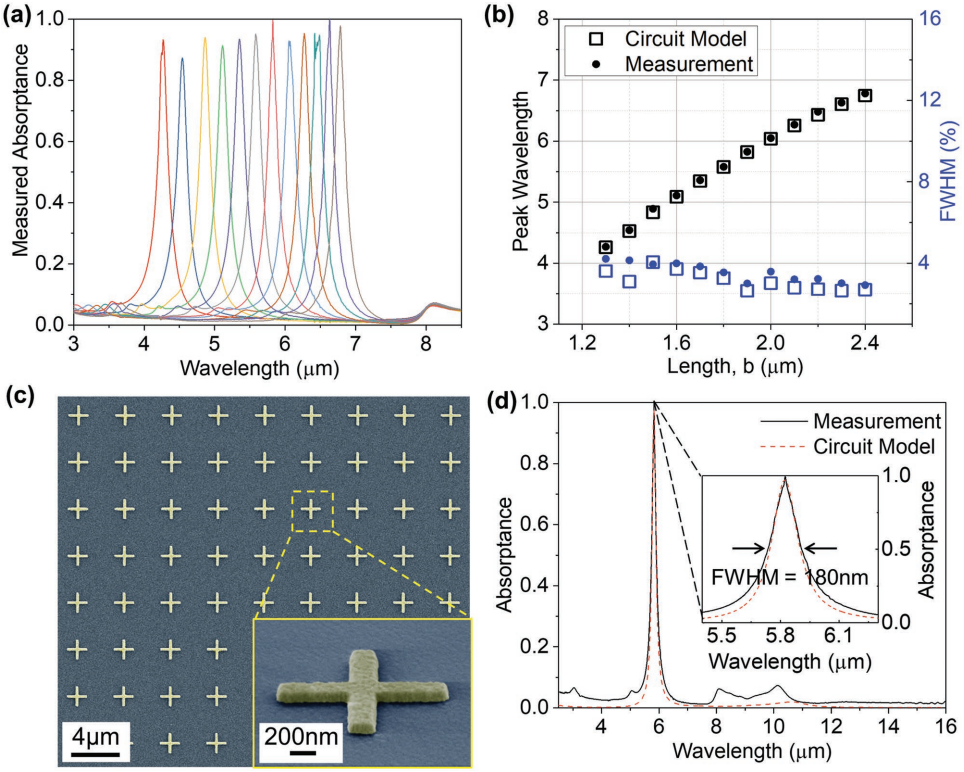

Figure 3. Experimental demonstration of narrowband MIM IR absorbers. a) Absorption spectra of the twelve narrowband MIM IR absorbers with lithographically tuned peak absorption. b) The experimental verification of peak wavelengths and FWHM of the 12 absorbers predicted by the circuit model. c) The false colored scanning electron microscopy (SEM) image of the ultra-narrow MIM IR absorber. The inset is a close-up SEM image of a cross-shaped nanostructure, highlighting no-residue lift-off fabrication process. d) The measured absorption spectrum (black solid line) of the absorber shown in (c) compared with the absorption spectrum predicted by the equivalent circuit model (red dashed line). The inset highlights the ultra-narrow FWHM reaching its theoretical limit of 3%. The lateral dimensions are as follows: Γ = 4.0 μm, a = 200 nm, and b = 1.9 μm.

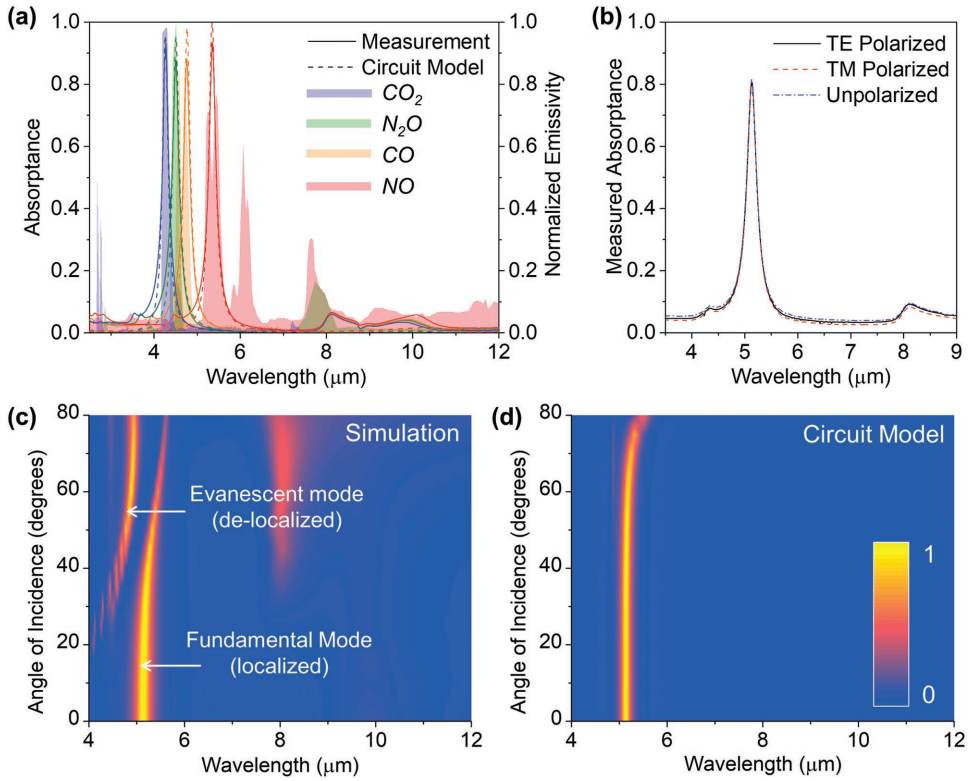

Figure 4. Narrowband MIM IR absorbers for MWIR spectroscopy. a) Graphical demonstration of nondisruptive MWIR gas spectroscopy based on the proposed narrowband MIM IR absorbers. b) Demonstration of polarization insensitivity with the measured absorption spectra of a fabricated MIM IR absorber with and without polarizers of FTIR microscope. c,d) Absorption color maps with respect to the angle of incidence and wavelengths obtained by numerical simulation (c) and circuit model (d).

To demonstrate the potential impact of this work for the development of high-resolution and miniaturized IR spectrometers and multispectral imagers, we examine the spectral selectivity of the proposed absorbers as well as their polarization and angular sensitivity, specifically for trace-gas sensing in MWIR. To highlight the capability of the proposed optimized narrowband MIM IR absorber to address the most stringent spectral resolution requirements for spectroscopy applications, the absorptances of four optimized narrowband MIM IR absorbers are compared with the normalized emission spectra of four heated gases taken from HITRAN and NIST Chemistry WebBook (**Figure 4**a)[51,52] The demonstrated ultrahigh spectral resolution allows each absorber to fully capture the IR signature of interest while rejecting the other densely located IR emissions. The calculated absorption spectra are also overlapped with the measurement results of the fabricated devices to further highlight the accuracy of the circuit model. The polarization independency was experimentally demonstrated by measuring absorption spectra upon TE, TM, and unpolarized (in the absence of a polarizer) incident waves using polarizers in Fourier transform infrared (FTIR) microscope (Figure 4b). Thanks to the fourfold symmetric cross-shaped nanostructures, the absorption is independent of polarization, evidenced by the three measured spectra with different polarizations perfectly overlapping with each other. Due to the limited range of incident angles set by the objective lens of FTIR microscope, the omnidirectional absorption is verified via equivalent circuit model and numerical calculation using Computer Simulation Technology, a commercial full-wave simulation software (Supporting Information). The full-wave simulation reveals that more than 70% absorption is maintained up to 60° of incident angle with little peak shift ($\Delta\lambda < 5\%$) (Figure 4c and d). The demonstrated robust angular response of the absorber is therefore suitable for various standoff spectroscopic sensing applications that the angle of incidence is not in a limited range. We believe that the discrepancy observed in the angular dependency of the fundamental mode between the simulation and the circuit model results from the onset of evanescent mode, which is not predicted by the circuit model.

In conclusion, we have presented the experimental demonstration and theoretical model of ultra-narrow bandwidth MIM IR absorbers specifically tailored for miniaturized mid-wavelength IR spectroscopy applications. The circuit model presented here provides an in-depth analysis of the spectral absorption response with respect to the constituent material and geometric parameters without the need of time-consuming numerical simulation. It is found that the cross-shaped nanostructures with a high length-to-width ratio and a wider periodicity result in maximized field confinement and reduced cross-talk, leading to the narrow absorption bandwidth reaching its limit, while maintaining a near unity absorption at peak wavelength. The fabricated devices consistently show narrow FWHM as small as 3.1%, with the peak absorption wavelength tunable in a

wide IR spectral region, while maintaining high absorptance ($\eta > 99.7\%$), wide acceptance angle, and polarization insensitivity. We believe that the demonstrated ultrahigh spectral resolution in the subwavelength thickness is a key enabler for a new class of miniaturized microsystems suitable for applications, such as noninvasive medical diagnosis, multispectral imaging, environmental monitoring, and military defense.

Experimental Section

Device Characterization: The reflectance spectra of the fabricated devices were measured using a Fourier transform infrared microscope (Bruker LUMOS FTIR Microscope). A reference measurement of the reflectance was first performed on the standard gold mirror. The raw reflectance measurements were then performed on the fabricated devices and normalized to the reference measurement in order to exclude atmosphere absorption. The size of knife-edge aperture was fixed at $\approx 100 \times 100\ \mu m^2$ for both reference and device measurements. Absorption (A) was calculated by $A = 1 - R - T \approx 1 - R$, where R is the measured reflectance and T is the transmittance. The transmitted power was assumed to be negligible ($T \approx 0$), as the ground layer (100 nm Au) of the fabricated absorbers was thicker than the penetration depth ($\delta_{Au} \approx 20$ nm) at the working IR wavelengths.

Supporting Information

Supporting Information is available from the Wiley Online Library or from the author.

Acknowledgements

The authors thank the staff of the George J. Kostas Nanoscale Technology and Manufacturing Research Center at Northeastern University and the Center for Nanoscale Systems at Harvard University where the devices were fabricated. This work was supported by NSF CAREER award no. ECCS-1350114, the DARPA NZERO Program contract no. HR0011-15-2-0048, and the Welch Foundation with grant no. F-1802.

Conflict of Interest

The authors declare no conflict of interest.

Keywords

infrared absorbers, metamaterials, microelectromechanical system, plasmonics, spectroscopy

Received: September 7, 2018
Revised: October 21, 2018
Published online: November 19, 2018

[1] A. Fried, D. Richter, *Analytical Techniques for Atmospheric Measurement*, Blackwell Publishing, Oxford, UK **2007**, 72–146.
[2] F. Tittel, D. Richter, A. Fried, *Solid-State Mid-Infrared Laser Sources* **2003**, *516*, 445.
[3] R. Adato, S. Aksu, H. Altug, *Mater. Today* **2015**, *18*, 436.
[4] M. Reichenbächer, J. Popp, *Challenges in Molecular Structure Determination*, Springer, Berlin/Heidelberg, Germany **2012**.
[5] A. De Luca, S. Z. Ali, R. Hopper, S. Boual, J. W. Gardner, F. Udrea, in *2017 IEEE 30th Int. Conf. Micro Electro Mech. Syst.*, IEEE, Piscataway, NJ, USA **2017**, 1220.
[6] J. T. Song, J. H. Park, J. K. Lee, J. C. Choi, S. H. Kong, *Jpn. J. Appl. Phys.* **2012**, *51*, 06FL18.
[7] T. Inoue, M. De Zoysa, T. Asano, S. Noda, *Appl. Phys. Express* **2014**, *7*, 012103.
[8] N. Engheta, *IEEE Antennas Propag. Soc. Int. Symp.*, Vol. *2* (IEEE Cat. No. 02CH37313), IEEE, Piscataway, NJ, USA **2002**, 392.
[9] C. M. Watts, *Ph.D. Thesis*, Boston College, Chestnut Hill, MA, USA **2015**.
[10] Z. Li, S. Butun, K. Aydin, *ACS Nano* **2014**, *8*, 8242.
[11] Y. Qu, Q. Li, H. Gong, K. Du, S. Bai, D. Zhao, H. Ye, M. Qiu, *Adv. Opt. Mater.* **2016**, *4*, 480.
[12] Y. L. Liao, Y. Zhao, *Plasmonics* **2015**, *10*, 1219.
[13] Y. L. Liao, Y. Zhao, X. Zhang, Z. Chen, *Opt. Commun.* **2017**, *385*, 172.
[14] D. Zhao, L. Meng, H. Gong, X. Chen, Y. Chen, M. Yan, Q. Li, M. Qiu, *Appl. Phys. Lett.* **2014**, *104*, 221107.
[15] W. Yue, Z. Wang, Y. Yang, J. Han, J. Li, Z. Guo, H. Tan, X.-X. Zhang, *Plasmonics* **2016**, *11*, 1557.
[16] N. Liu, M. Mesch, T. Weiss, M. Hentschel, H. Giessen, *Nano Lett.* **2010**, *10*, 2342.
[17] C. M. Watts, X. Liu, W. J. Padilla, *Adv. Mater.* **2012**, *24*, OP98.
[18] X. Liu, *Ph.D. Thesis*, Boston College **2013**.
[19] Y. Cui, Y. He, Y. Jin, F. Ding, L. Yang, Y. Ye, S. Zhong, Y. Lin, S. He, *Laser Photonics Rev.* **2014**, *8*, 495.
[20] S. Kang, Z. Qian, V. Rajaram, A. Alu, M. Rinaldi, in *2017 19th Int. Conf. Solid-State Sensors, Actuators, and Microsystems*, IEEE, Piscataway, NJ, USA **2017**, 886–889.
[21] T. Maier, H. Brückl, *Opt. Lett.* **2009**, *34*, 3012.
[22] T. Maier, H. Brueckl, *Opt. Lett.* **2010**, *35*, 3766.
[23] J.-Y. Jung, J. Lee, D.-G. Choi, J.-H. Choi, J.-H. Jeong, E.-S. Lee, D. P. Neikirk, *IEEE Photonics J.* **2015**, *7*, 1.
[24] M. Breen, W. Streyer, R. Lu, A. Gao, D. Wasserman, S. Gong, in *2016 IEEE Int. Freq. Control Symp.*, IEEE, Piscataway, NJ, USA **2016**, 1–6.
[25] Y. Hui, J. S. Gomez-Diaz, Z. Qian, A. Alù, M. Rinaldi, *Nat. Commun.* **2016**, *7*, 11249.
[26] Z. Qian, S. Kang, V. Rajaram, M. Rinaldi, in *2016 IEEE SENSORS*, IEEE, Piscataway, NJ, USA **2016**, 1–3.
[27] Z. Qian, S. Kang, V. Rajaram, C. Cassella, N. E. McGruer, M. Rinaldi, *Nat. Nanotechnol.* **2017**, *12*, 969.
[28] V. Rajaram, Z. Qian, S. Kang, C. Cassella, N. E. McGruer, M. Rinaldi, in *2017 19th Int. Conf. Solid-State Sensors, Actuators, and Microsystems*, IEEE, Piscataway, NJ, USA **2017**, 846–849.
[29] Z. Qian, S. Kang, V. Rajaram, C. Cassella, N. E. McGruer, M. Rinaldi, in *2017 IEEE 30th Int. Conf. Micro Electro Mech. Syst.*, IEEE, Piscataway, NJ, USA **2017**, 940–941.
[30] A. Lochbaum, Y. Fedoryshyn, A. Dorodnyy, U. Koch, C. Hafner, J. Leuthold, *ACS Photonics* **2017**, *4*, 1371.
[31] T. D. Dao, S. Ishii, T. Yokoyama, T. Sawada, R. P. Sugavaneshwar, K. Chen, Y. Wada, T. Nabatame, T. Nagao, *ACS Photonics* **2016**, *3*, 1271.
[32] X.-Y. Peng, B. Wang, S. Lai, D. H. Zhang, J.-H. Teng, *Opt. Express* **2012**, *20*, 27756.
[33] A. Sakurai, B. Zhao, Z. M. Zhang, *J. Quant. Spectrosc. Radiat. Transfer* **2014**, *149*, 33.
[34] A. Sakurai, B. Zhao, Z. M. Zhang, in *Proc. 15th Int. Heat Transf. Conf.*, **2014**, 1–10.
[35] S. A. Tretyakov, C. R. Simovski, *J. Electromagn. Waves Appl.* **2003**, *17*, 131.

[36] J. Nath, S. Modak, I. Rezadad, D. Panjwani, F. Rezaie, J. W. Cleary, R. E. Peale, *Opt. Express* **2015**, *23*, 20366.
[37] J. D. Jackson, *Classical Electrodynamics*, Wiley, New York **1975**.
[38] J. Kischkat, S. Peters, B. Gruska, M. Semtsiv, M. Chashnikova, M. Klinkmüller, O. Fedosenko, S. Machulik, A. Aleksandrova, G. Monastyrskyi, Y. Flores, W. Ted Masselink, *Appl. Opt.* **2012**, *51*, 6789.
[39] N. Engheta, A. Salandrino, A. Alù, *Phys. Rev. Lett.* **2005**, *95*, 095504.
[40] A. Alù, A. Salandrino, N. Engheta, *J. Opt. Soc. Am. B* **2007**, *24*, 3014.
[41] B. A. Munk, *Frequency Selective Surfaces*, Wiley, Hoboken, NJ, USA **2000**.
[42] Y. P. Lee, J. Y. Rhee, Y. J. Yoo, K. W. Kim, *Metamaterials for Perfect Absorption*, Springer, Singapore **2016**.
[43] Y. Zhong, D. Wasserman, Y. Zhong, S. D. Malagari, T. Hamilton, D. Wasserman, *J. Nanophotonics* **2015**, *9*, 093791.
[44] A. D. Rakić, A. B. Djurišić, J. M. Elazar, M. L. Majewski, *Appl. Opt.* **1998**, *37*, 5271.
[45] S. A. Maier, *Plasmonics: Fundamentals and Applications*, Springer, New York **2007**.
[46] D. R. Smith, S. Schultz, P. Markoš, C. M. Soukoulis, *Phys. Rev. B* **2002**, *65*, 195104.
[47] X. Zhang, Y. Wu, *Sci. Rep.* **2015**, *5*, 7892.
[48] J. Pendry, A. Holden, W. Stewart, I. Youngs, *Phys. Rev. Lett.* **1996**, *76*, 4773.
[49] J. B. Pendry, A. J. Holden, D. J. Robbins, W. J. Stewart, *IEEE Trans. Microwave Theory Tech.* **1999**, *47*, 2075.
[50] R. S. Longhurst, *Geometrical and Physical Optics*, Wiley, New York **1967**.
[51] L. S. Rothman, I. E. Gordon, A. Barbe, D. C. Benner, P. F. Bernath, M. Birk, V. Boudon, L. R. Brown, A. Campargue, J. P. Champion, K. Chance, L. H. Coudert, V. Dana, V. M. Devi, S. Fally, J. M. Flaud, R. R. Gamache, A. Goldman, D. Jacquemart, I. Kleiner, N. Lacome, W. J. Lafferty, J. Y. Mandin, S. T. Massie, S. N. Mikhailenko, C. E. Miller, N. Moazzen-Ahmadi, O. V. Naumenko, A. V. Nikitin, J. Orphal, V. I. Perevalov, A. Perrin, A. Predoi-Cross, C. P. Rinsland, M. Rotger, M. Šimečková, M. A. H. Smith, K. Sung, S. A. Tashkun, J. Tennyson, R. A. Toth, A. C. Vandaele, J. Vander Auwera, *J. Quant. Spectrosc. Radiat. Transfer* **2009**, *110*, 533.
[52] P. J. Listrom, W. G. Mallard, *NIST Chemistry WebBook*, http://webbook.nist.gov/chemistry/ (accessed: August 2017).